Zeng et al. Nanoscale Research Letters (2017) 12:13
DOI 10.1186/s11671-016-1783-0

Nanoscale Research Letters

NANO EXPRESS Open Access

Enhancement of Electrochemical Performance by the Oxygen Vacancies in Hematite as Anode Material for Lithium-Ion Batteries

Peiyuan Zeng[1], Yueying Zhao[1], Yingwu Lin[2], Xiaoxiao Wang[1], Jianwen Li[1], Wanwan Wang[1] and Zhen Fang[1,3*]

Abstract

The application of hematite in lithium-ion batteries (LIBs) has been severely limited because of its poor cycling stability and rate performance. To solve this problem, hematite nanoparticles with oxygen vacancies have been rationally designed by a facile sol–gel method and a sequential carbon-thermic reduction process. Thanks to the existence of oxygen vacancies, the electrochemical performance of the as-obtained hematite nanoparticles is greatly enhancing. When used as the anode material in LIBs, it can deliver a reversible capacity of 1252 mAh g^{-1} at 2 C after 400 cycles. Meanwhile, the as-obtained hematite nanoparticles also exhibit excellent rate performance as compared to its counterparts. This method not only provides a new approach for the development of hematite with enhanced electrochemical performance but also sheds new light on the synthesis of other kinds of metal oxides with oxygen vacancies.

Keywords: Hematite, Oxygen vacancies, Calcination, Lithium-ion batteries

Background

Because of its high theoretical capacity, natural abundance, and environmental friendliness, hematite (α-Fe_2O_3) has been regarded as a promising anode material for lithium-ion batteries (LIBs) [1–4]. However, the practical application of hematite is greatly limited because of its low conductivity, large volume variation, and easy aggregation during the discharge/charge process [5–9]. To overcome these drawbacks, two main methods are employed. The first method concerns on the synthesis of nano-sized iron oxides with different structures, which will shorten the transportation distances of electron and Li^+. The second method focuses on elevating the conductivity of hematite, which is mainly realized by forming the composite between hematite and materials with high electronic conductivity [10–14]. Despite these progresses, a simpler method for the preparation of hematite with enhanced electrochemical performance is still needed when considering its practical uses.

The introduction of oxygen vacancies into metal oxides has been proved to be an effective method to modulate the intrinsic electrochemical properties of the metal oxides [15, 16]. The existence of oxygen vacancies could effectively change the electronic structure of the metal oxides, reduce the energy requirement for electron or ion diffusion, and lower the resistance, which could be beneficial to improve the electrochemical performances of the metal oxides [17]. What is more, previous reports also clearly indicate that the existence of oxygen vacancies could facilitate the phase transition and reduce the stress during Li^+ insertion/depletion, which will be helpful to improve the rate performance as well as the cycling stabilities of the electrode materials. Oxygen vacancies could also provide more physical space for Li^+ storage thus improving the specific capacity of the materials [18, 19]. For this reason, a large number of efforts have been devoted to the synthesis of electrode material with oxygen vacancies, all of which have shown enhanced electrochemical

* Correspondence: fzfscn@mail.ahnu.edu.cn
[1]Key Laboratory of Functional Molecular Solids, Ministry of Education, Center for Nano Science and Technology, College of Chemistry and Materials Science, Anhui Normal University, Wuhu 241000, People's Republic of China
[3]Present address: East Beijing Road 1#, Wuhu, Anhui Province, People's Republic of China
Full list of author information is available at the end of the article

performance when used in LIBs. For example, $Li_3VO_{4-\delta}$ was synthesized by annealing Li_3VO_4 powders in vacuum, and the introduction of oxygen vacancies lead to the enhanced initial coulombic efficiency, reversible capacity, and cycling stability [20]. The as-synthesized $Li_3VO_{4-\delta}$ delivers a reversible capacity of 247 mAh g^{-1} after 400 cycles at 500 mA g^{-1}, which is much higher than the corresponding value of pristine Li_3VO_4 (64 mAh g^{-1}). MoO_{3-x} nanosheets were synthesized by oxidizing Mo powers in the atmosphere containing H_2O_2 and absolute ethanol. The as-prepared materials exhibit fascinating reversible capacity and long-term cycling stability (179.3 mAh g^{-1} at 1 A g^{-1}) when used as anode materials for sodium ion batteries [18]. Anatase $TiO_{2-\delta}$–carbon nanotubes (CNTs) composites were prepared by a two-step CVD method. The CNT grown on TiO_2 leads to the formation of oxygen vacancies under the reducing atmosphere, which greatly enhanced the electrochemical performance, especially the rate performance. The half cells cycled at 30 C can still deliver a capacity of more than 40 mAh g^{-1} [21]. V_2O_5 nanosheets with oxygen vacancies were also prepared by a hydrothermal reaction [22]. The as-prepared H-V_2O_5 electrode exhibits excellent cycling stability and improved rate capability, which could be mainly attributed to the introduction of oxygen vacancies. Tong and his co-workers proposed a facile method to generate oxygen vacancies into the materials by slight nitridation in NH_3 atmosphere [23, 24]. Using this method, hematite and titanium dioxide with oxygen vacancies had been successfully synthesized and delivered enhanced cyclability and rate performance. Additionally, TiO_2 heterostructured nanosheet was synthesized by hydrogenation process. This kind of heterostructured nanosheet delivered a fascinating electrochemical performance. When it was used as anode material in full battery, the full battery could achieve high energy and power density [25].

Thus, it is reasonable to believe that the electrochemical performance of hematite in LIBs could be effectively enhanced by the introduction of oxygen vacancies. However, few report concerning on the effect of oxygen vacancies in hematite has been published in the field of LIBs to date. Meanwhile, the reported method for the preparation of oxygen defect α-Fe_2O_3 are usually based on the thermal decomposition of FeOOH in the inert gas or in vacuum, which usually needs tedious procedure and complex equipment. In this work, we present a facile method for the synthesis of α-Fe_2O_3 with oxygen vacancies via a two-step process incorporating a sol–gel synthesis of the precursor and thermal annealing of the precursor in air. In this synthetic route, the precursor was synthesized by a sol–gel method and then calcined in air to yield α-Fe_2O_3 nanoparticles with oxygen vacancies. The partial reduction of Fe(III) during the carbon-thermic process leads to the formation of oxygen vacancies in the final product, which has also been reported for the synthesis of titanium dioxide with oxygen vacancies [21, 26]. Compared with the previous reports, the preparation of α-Fe_2O_3 nanoparticles with oxygen vacancies is more simple, which will lower the cost during the production process. What is more, this method can be easily scaled up by simply increasing the initial amount of the starting material. These two fascinating characteristics make this method suitable for the large-scale application in the future. Thanks to the oxygen vacancies, the electrochemical performance of α-Fe_2O_3 is greatly promoted. Remarkably, the as-prepared $Fe_2O_{3-\delta}$ still maintained a reversible capacity of 1252 mAh g^{-1} at 2 C after 400 cycles. Meanwhile, the as-obtained $Fe_2O_{3-\delta}$ also exhibit excellent rate performance. Even being cycled at 40 C, the as-prepared electrode material can still deliver a discharge capacity of 188 mAh g^{-1}, which is much higher than the corresponding value than the reported α-Fe_2O_3 electrode material. This synthetic method not only provides a new method for the enhancement of hematite-based electrode materials but also sheds a new light for the preparation of metal oxides with oxygen vacancies.

Methods

Synthesis of $Fe_2O_{3-\delta}$ Nanoparticles

In a typical procedure, 2 mmol $FeCl_3{\cdot}6H_2O$ and 4 mmol urea were dissolved in 46 mL distilled water with continuous stirring. Then, 4 mL acrylic acid was added into the as-formed yellow solution. In the next step, the mixed solution was transferred into a 70-mL Teflon-lined stainless steel autoclave and maintained at 140 °C for 12 h. After cooling down to room temperature, the gel-like product was collected by centrifugation, washed with distilled water and absolute alcohol several times and then dried in an oven at 80 °C overnight. To obtain hematite with oxygen vacancies, the as-formed precursor was calcined at 350 °C for 1.5 h in air with a heating rate of 2 °C min^{-1}.

Sample Characterizations

The morphology and structure of the sample was investigated by transmission electron microscopy (TEM, Hitachi HT 7700) and high-resolution TEM (HRTEM, JEOL-2010). X-ray diffraction patterns were obtained using a Bruker D8 Advance with Cu-K_α radiation. X-ray photoelectron spectra (XPS) of the samples were recorded on an ESCALAB 250. The thermogravimetric analysis (TGA) was carried out on SDT 2960 with a heating rate of 10 °C min^{-1} from 20 to 600 °C. The BET surface area was determined on an ASAP 2460 sorption apparatus. All the as-prepared samples were degassed at 150 °C for 10 h prior to nitrogen adsorption measurements. Electron paramagnetic resonance (EPR) tests were carried out on a Bruker A300 spectrometer (X-band, frequency 9.43 GHz) equipped with Bruker ER4141VTM liquid nitrogen system. The microwave power was 0.595 mW

and modulation amplitude 3.0 G. The samples were measured at 90 K with center field 3500 G and sweep width 5000 G.

Electrochemical Measurements

The electrochemical measurements were performed on coin-type cells (CR2032). The electrode was prepared using active material, acetylene black (Super P), and polyvinylidene fluoride (PVDF) in a weight ratio of 6:2:2. The electrolyte was a solution of 1 M $LiPF_6$ in a mixture of EC:DEC (1:1 by volume). The cells were assembled in in an argon-filled glovebox (Mikrouna, Super (1220/750/900)) with both moisture and oxygen concentrations below 0.1 ppm. The galvanostatic discharge/charge characteristics were tested in the potential window of 0.01 to 3.0 V using a Neware battery tester. Cyclic voltammetry (CV) and electrochemical impedance spectroscopy (EIS) were tested on a CHI660E electrochemical workstation.

Results and Discussion

The hydrothermal process at 140 °C for 12 h will lead to the formation of the gel-like precursor, which will be used as the starting material for the preparation of hematite with oxygen vacancies. The corresponding XRD pattern of the precursor (Additional file 1: Figure S1a) clearly indicates that the precursor is mainly composed of FeOOH (JCPDS No. 29–0713), which is obtained by the hydrolysis of Fe^{3+} in the solution. The TEM observation of the precursor (Additional file 1: Figure S1b) further confirms that the as-formed nanoparticles are wrapped in a gel-like matrix. To get further insight into the composition of the precursor, FT-IR was employed and the corresponding result is shown in Additional file 1: Figure S2. The corresponding result clearly indicates the formation of polyacrylic acid (PAA). The absorption bands centering at 1634 and 984 cm^{-1} could be attributed to the C=C and $=CH_2$, respectively. And the absorption band at 1705 cm^{-1} can be assigned to the C=O double bond vibration of COOH groups [27, 28]. And the formation of PAA could be proved according to the disappearance of the absorption bands centering at 1634 and 984 cm^{-1}, which has been widely reported in the previous reports [29]. Thus, the as-obtained precursor could be regarded as a nanocomposite forming by dispersing the FeOOH nanoparticles in the matrix of PAA.

For the formation of hematite with oxygen vacancies, an in situ carbon-thermic process was employed. This process can be divided into two steps: (i) the carbonization process of PAA; (ii) the transformation of FeOOH to hematite and thermal reduction of hematite with the as-formed carbon in the first step. To understand good control of the in situ carbon-thermic process, thermogravimetric analysis was employed as a guide here (Fig. 1). The total weight loss during the heating process is about

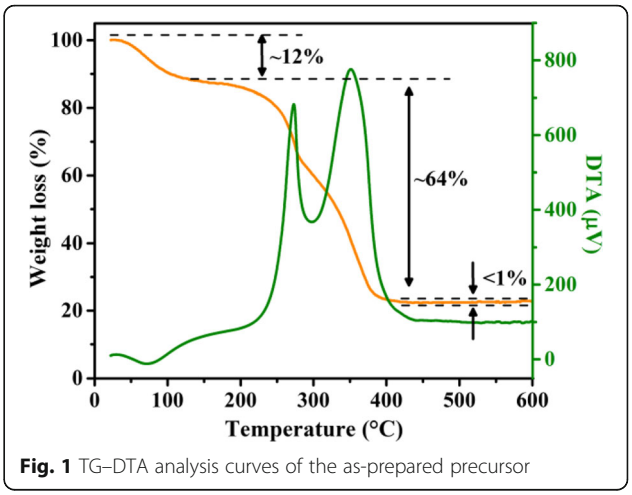

Fig. 1 TG–DTA analysis curves of the as-prepared precursor

76%, indicating the high content of organic compounds in the precursor. The first stage of weight loss below 150 °C is about 12%, which can be ascribed to the evaporation of water molecules in the gel-like precursor. A major weight loss can be observed in the temperature range between 200 and 400 °C, which can be ascribed to the carbonization of PAA, the decomposition of FeOOH, the partial reduction of the as-formed hematite, and combustion of the as-formed carbon, respectively. Less than 1% weight loss can be observed as the temperature is higher than 450 °C, indicating the burnout of carbon. The DTA analysis curve has two exothermic peaks locating at 273 and 350 °C. The first exothermic peak can be ascribed to the carbonization of the organic component, while the second exothermic peak may correspond to the formation of hematite and carbon-thermic reduction of hematite. During the heating progress, the corundum crucible was filled with CO_2, which would provide a hypoxic environment and lead to the formation of α-Fe_2O_3 with oxygen vacancies.

According to the above analysis, the carbon-thermic reduction process during the calcination process may also lead to the formation of impurities such as Fe_3O_4 or carbon in the final product. To exclude the existence of Fe_3O_4 or carbon, both XRD and Raman spectra were employed. Figure 2a is the XRD pattern of the as-prepared sample, on which all the diffraction peaks can be indexed to be the rhombohedral-phased α-Fe_2O_3 (JCPDS No. 33–0664). No other diffraction peaks belonging to C or Fe_3O_4 is detected, indicating high purity of the sample. To further exclude the existence of C or Fe_3O_4, the Raman spectrum was employed and the result is shown in Fig. 2b. The peaks locating at 227, 293, 408, 496, 608, 658, and 1315 cm^{-1} are the typical peaks for α-Fe_2O_3, indicating the formation of rhombohedral-phased α-Fe_2O_3. The peaks centering at 227 and 496 cm^{-1} correspond to the A_{1g} modes of α-Fe_2O_3,

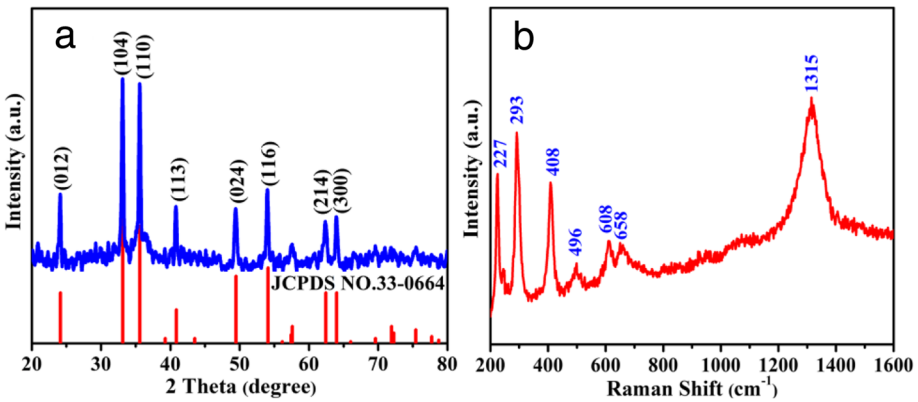

Fig. 2 **a** XRD pattern of the obtained sample. **b** Raman spectra of $Fe_2O_{3-\delta}$

while the peaks centered at 293, 408, and 608 cm^{-1} can be assigned to the E_g modes of α-Fe_2O_3 [30]. The peak locating at 658 cm^{-1} could be attributed to the disorder effects or the presence of hematite nanocrystals [31, 32]. The broad peak centered at 1315 cm^{-1} can be assigned to the two-magnon scattering which results from the interaction between two magnons [33]. No peaks can be found at 1350 and 1580 cm^{-1}, which indicates the absence of carbon in the sample [34]. Meanwhile, the typical Raman peaks for Fe_3O_4 are also not detected, indicating that the as-obtained sample is α-Fe_2O_3.

The overall XPS spectrum of the as-prepared sample is shown as Fig. 3a, which clearly reveals the presence of oxygen vacancies in the as-obtained product. As it is shown in Fig. 3b, the peak centering at 710.8 and 724.3 eV are the characteristic peaks of Fe^{3+} in hematite [35–38]. The existence of oxygen vacancies in the as-prepared sample can be proved according to the XPS spectrum of O1s

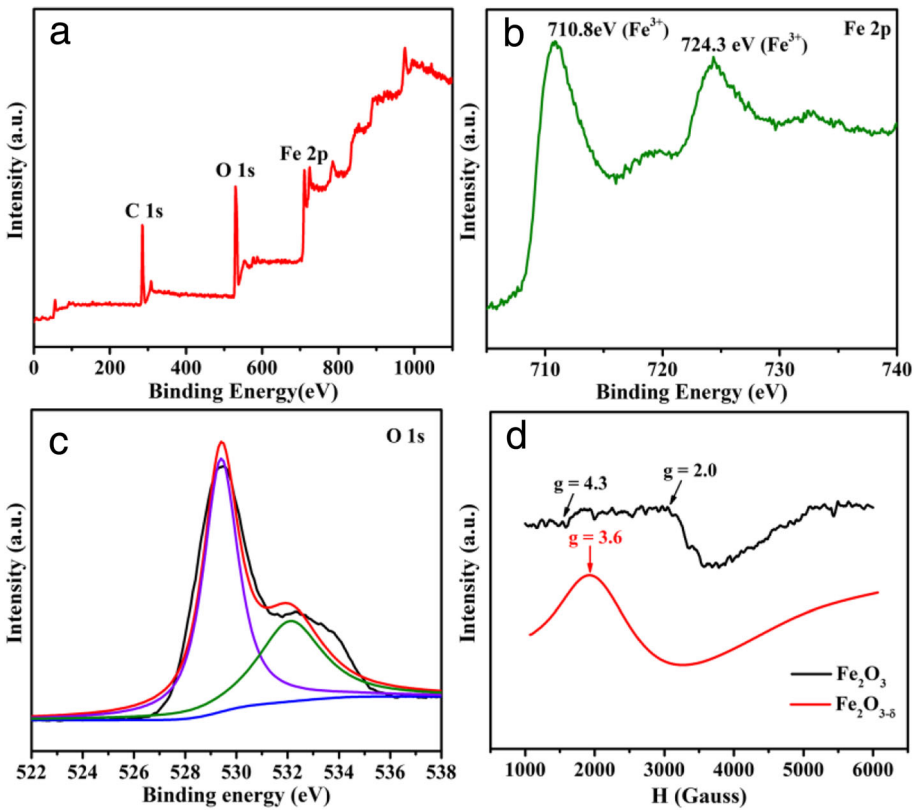

Fig. 3 **a** The wide-survey, **b** Fe 2p, and **c** O 1s XPS spectra of $Fe_2O_{3-\delta}$. **d** EPR spectra of $Fe_2O_{3-\delta}$ collected at 90 K, where *H* is the magnetic field

(Fig. 3c). The peak locating at 529.4 eV could be ascribed to the lattice oxygen of hematite, while the peak centering at 532.1 eV is associated with the oxygen vacancies in hematite [39–42]. To further confirm the existence of oxygen vacancies in the as-prepared materials, EPR spectra of $Fe_2O_{3-\delta}$ was employed (Fig. 3d). For comparison purpose, the EPR spectrum of the commercial α-Fe_2O_3 is also recorded. As it is shown in Fig. 3d, the commercial α-Fe_2O_3 shows EPR signals at $g = 2.0$ and $g = 4.3$, which could be attributed to Fe^{3+} ions coupled by exchange interactions and Fe^{3+} ions in rhombic and axial symmetry sites, respectively [43, 44]. Because Fe^{2+} ions are not directly involved in the EPR absorption, it only shows a single broad resonance line centered at about $g = 3.6$. This phenomenon can be attributed to the interactions between Fe^{2+} ions and Fe^{+3} ions, which will influence the lines shape as a result. Based on the above characterizations, the existence of oxygen vacancies can be clearly proved. Thus, the chemical formula of the as-obtained product could be described as α-$Fe_2O_{3-\delta}$ [43, 44].

According to the TEM observation (Fig. 4a), the as-prepared sample is composed of a large number of nanoparticles, with diameters ranging from ~5 to 20 nm. Meanwhile, the as-prepared α-$Fe_2O_{3-\delta}$ sample is mesoporous according to the TEM observation. The typical lattice distance is determined to be 0.27 nm for the as-prepared sample, which corresponds to the $(10\bar{1}4)$ lattice plane (Fig. 4b). This result further confirms that the as-prepared sample is rhombohedral phased α-Fe_2O_3. The porous nature of the as-prepared α-$Fe_2O_{3-\delta}$ sample is further proved by the nitrogen adsorption–desorption experiment. The BET surface area of the as-prepared α-$Fe_2O_{3-\delta}$ sample is determined to be 54.58 $m^2\ g^{-1}$. And the BJH pore size distribution centers at about 6 nm, corresponding to the interspaces between these nanoparticles (Additional file 1: Figure S3).

The electrochemical behavior of the as-prepared α-$Fe_2O_{3-\delta}$ was firstly studied by the CV measurements at a scanning rate of 0.1 mV s^{-1}, with the potential window from 0.01 to 3.0 V (Fig. 5a). In the first cycle, two cathodic peaks at 1.6 and 0.72 V can be observed, which corresponds to the insertion of Li^+ into α-$Fe_2O_{3-\delta}$ and the reduction of $Fe_2O_{3-\delta}$ into metallic Fe. In the anodic progress, a broaden peak (between 1.6 and 1.9 V) and an ambiguous peak (at 2.3 V) can be observed, corresponding to the electrochemical oxidation reaction of metallic Fe to Fe^{2+} and Fe^{3+}, respectively [34]. In the second and third cycles, the cathodic peak shifts from 0.72 to 0.79 V, and the intensity greatly decreases, which may result from the decomposition of the electrolyte and formation of the solid electrolyte interphase (SEI) layer in the first cycle [45–49]. The CV plots overlap in the following cycles, indicating the excellent reversibility of the materials. The electrochemical reaction of this process can be expressed as follows:

$$Fe_2O_{3-\delta} + x\,Li^+ + x\,e^- \rightarrow Li_xFe_2O_{3-\delta} \quad (1)$$

$$Li_xFe_2O_{3-\delta} + (2-x)\,Li^+ + (2-x)\,e^- \rightarrow Li_2Fe_2O_{3-\delta} \quad (2)$$

$$Li_2Fe_2O_{3-\delta} + (4-2\delta)\,Li^+ + (4-2\delta)\,e^- \rightarrow 2Fe^0 + (3-\delta)\,Li_2O \quad (3)$$

Figure 5b is the initial three discharge/charge curves of α-$Fe_2O_{3-\delta}$ at a current density of 2 C. The initial discharge/charge capacities for the as-prepared α-$Fe_2O_{3-\delta}$ are 1863/1296 mAh g^{-1}, respectively. According to previous reports, oxygen vacancies are easily re-oxidized over

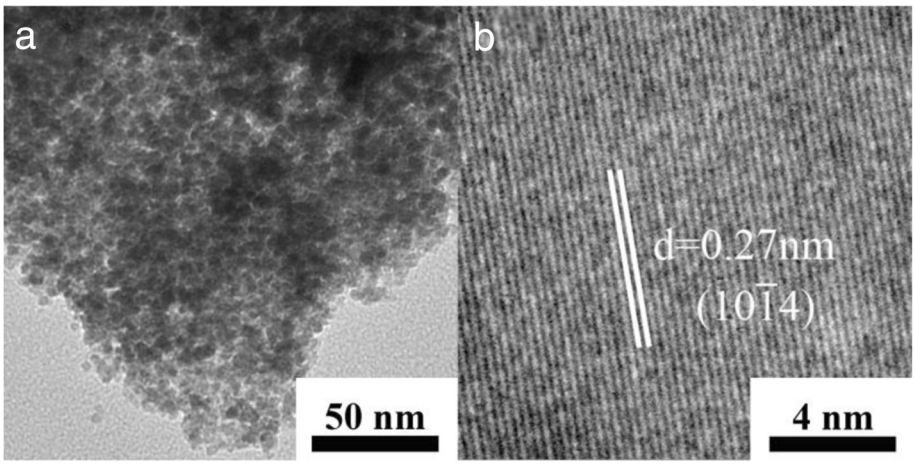

Fig. 4 **a** TEM image of the as-prepared $Fe_2O_{3-\delta}$ and **b** the corresponding HRTEM image

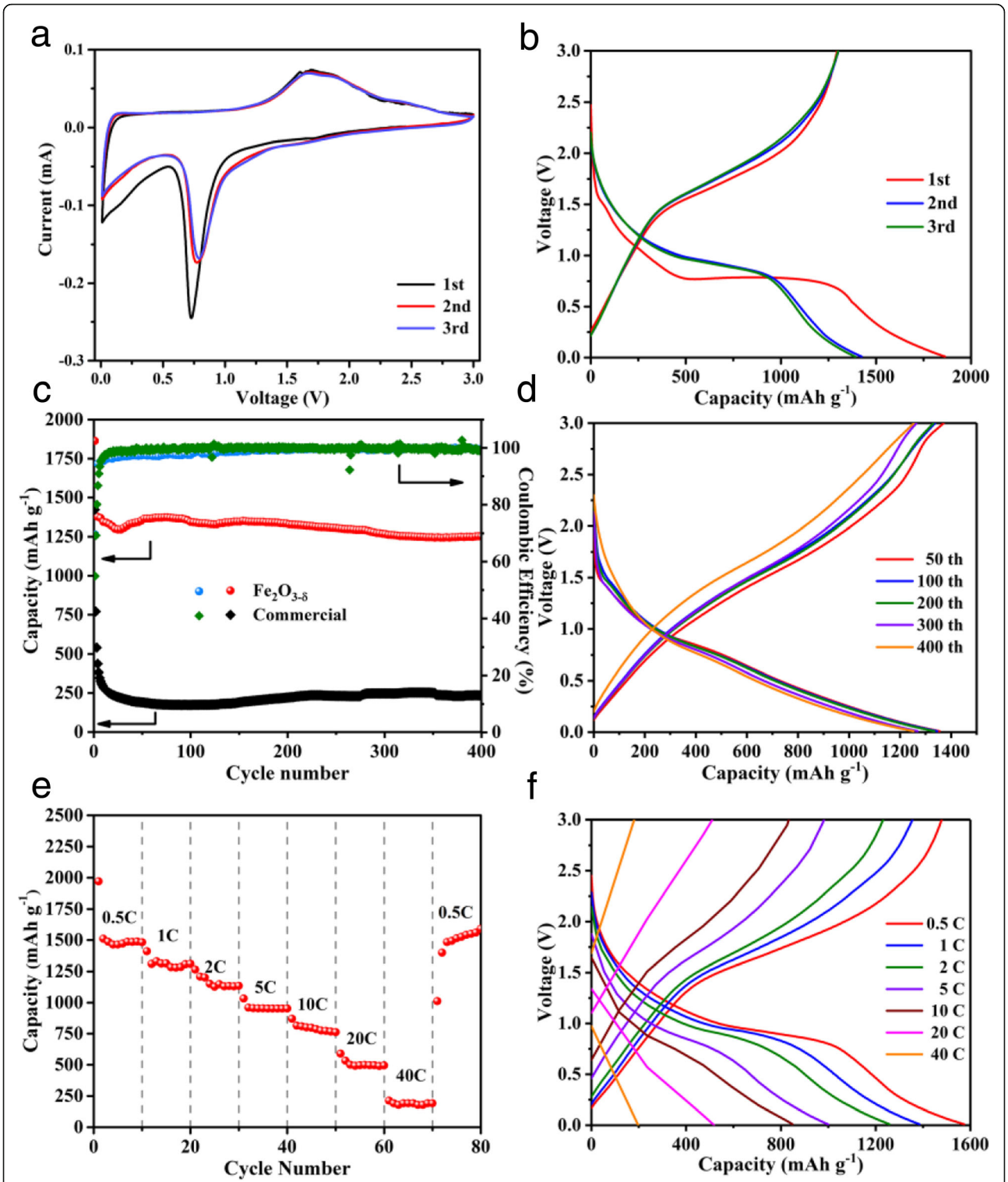

Fig. 5 **a** CV curves of the as-prepared $Fe_2O_{3-\delta}$. **b** The initial three galvanostatic charge/discharge profiles of $Fe_2O_{3-\delta}$. **c** Cycling performance and coulombic efficiencies of $Fe_2O_{3-\delta}$ and commercial Fe_2O_3 at 2 C. **d** Typical charge/discharge curves of $Fe_2O_{3-\delta}$ sample during long-term cycles at 2 C. **e** Rate performance of $Fe_2O_{3-\delta}$ at various current densities. **f** Charge/discharge curves of $Fe_2O_{3-\delta}$ sample at different current densities

time and the high conductivity also gradually diminishes [16]. Nevertheless, the as-prepared $Fe_2O_{3-\delta}$ sample in this work exhibits excellent cycling stability during the charge/discharge process (Fig. 5c). On the contrary, commercial Fe_2O_3 delivers a low initial coulombic efficiency and poor cyclability. Only about 250 mAh g^{-1} discharge capacity could be maintained after 20 cycles under identical condition. In initial several cycles, the electrodes of $Fe_2O_{3-\delta}$ show a slight decrease in capacity, which can be ascribed to the slow formation rate of complete SEI layer at high current density. Typical charge/discharge curves of the $Fe_2O_{3-\delta}$ sample during long-term cycles is shown in Fig. 5d. Only slight capacity decay could be found in the whole test process. And after 400 cycles at 2 C, the discharge capacity is about 1252 mAh g^{-1}, which is higher than the theoretical value of hematite (1007 mAh g^{-1}). The excessive capacity can be explained from several aspects. On one hand, the materials were obtained by calcination, which will lead to the formation of lattice defects in the typical nanostructure. These lattice defects will provide more active sites for Li^+ insertion/extraction, which could improve the specific capacity of the materials [50]. On the other hand, the decomposition and reformation of the SEI layer will also lead to the increase in capacity [51], but the central aspect is that the introduction of oxygen vacancies in the materials, which will provide more physical space for Li^+ storage, changes the intrinsic property of the sample and leads to the higher specific capacity than theoretical value.

The as-prepared α-$Fe_2O_{3-\delta}$ also exhibits fascinating rate performance during the charge/discharge cycles when the current density increased from 0.5 to 40 C in a stepwise manner and then returned to 0.5 C (Fig. 5e). The average reversible capacities of α-$Fe_2O_{3-\delta}$ were 1549, 1389, 1258, 995, 848, and 556 mAh g^{-1} at the discharge rate of 0.5, 1, 2, 5, 10, and 20 C, respectively. It is worth noting that the as-obtained α-$Fe_2O_{3-\delta}$ can still deliver a reversible capacity of 198 mAh g^{-1} at a high current density of 40 C. As the current density increased, the discharge/charge plat becomes ambiguous, indicating the redox reaction mainly occurred on the surface of the electrode materials other than the inside of the material (Fig. 5f). An average discharge capacity as high as 1590 mAh g^{-1} can maintain when the current rate returned to 0.5 C. This result clearly demonstrates that the as-obtained α-$Fe_2O_{3-\delta}$ is a good candidate for the potential application as high-rate anode materials for LIBs.

To further understand the discharge/charge storage mechanism of the as-prepared materials, CV measurements of α-$Fe_2O_{3-\delta}$ cells after 50 cycles were carried out at different scan rates, and the corresponding is shown in Fig. 6a. As the scan rates increase, the cathodic and anodic peaks shift to lower and higher potentials with increasing peak currents. The migratory peaks indicate the kinetics of Li^+ insertion/extraction at the electrode–electrolyte interfaces. However, the increasing peak currents are not proportional to the square root of the scan rate, which indicates that the discharge/charge progresses are composed of non-Faradaic and Faradaic behavior [52–54]. And the relationship between peak current (i) and scan rate (v) can be expressed as follows:

$$i = av^b \tag{4}$$

$$\log(i) = b\log(v) + \log(a), \tag{5}$$

where i is the peak current, v is the scan rate, and a and b are the adjustable parameters. The type of discharge/charge progresses can be determined by the value of b. When $b = 1$, the progresses mainly rely on pseudo-capacitive control, and when $b = 0.5$, the progresses are dependent on ionic diffusion. The linear relationship between log (i) and log (v) is shown in Fig. 6b. The b values (the slopes of the four lines) of the four redox peaks are 0.97, 0.86, 0.99, and 0.77, which means the electrochemical reactions of α-$Fe_2O_{3-\delta}$ are controlled by pseudo-capacitive behavior. The result is in good

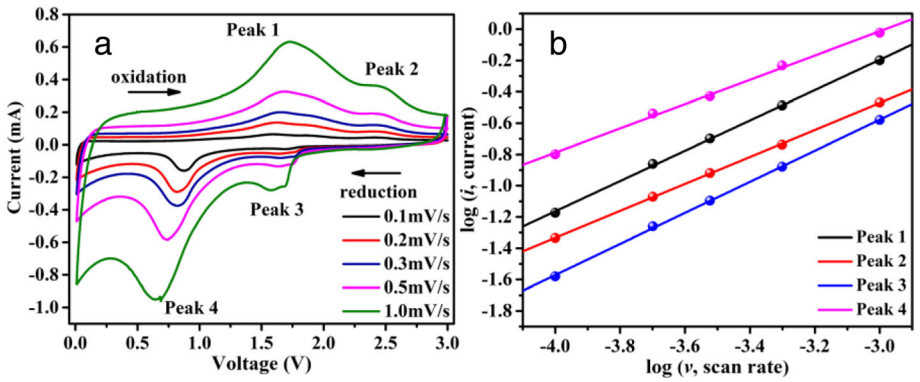

Fig. 6 a CV curves at different scan rates after 50 cycles. **b** Log (i) versus log (v) plots at different redox states of the as-prepared $Fe_2O_{3-\delta}$

accordance with the cycling performance. And it can also be employed to explain the reason why α-$Fe_2O_{3-\delta}$ has a high reversible specific capacity even cycled at 2C.

The EIS of the electrodes were performed to illustrate the effect of oxygen vacancies in sample α-$Fe_2O_{3-\delta}$. The Nyquist plots of the electrodes before cycling and after 400 cycles are shown in Additional file 1: Figure S4 with a frequency ranging from 100 to 0.01 H_z. The Nyquist plots are composed of semicircle in the high-to-middle frequency regions and a sloping long line in the low frequency region. The smaller diameter of the semicircle indicates lower contact resistance and charge transfer resistance. The more sloping long line indicates faster kinetics during cycles. Compared with the commercial hematite, $Fe_2O_{3-\delta}$ delivers a lower contact resistance and charge transfer resistance. This mainly ascribes to the introduction of oxygen vacancies, which could be regarded as electron donor, change the electronic structure, and facilitate the Li^+ ion diffusion and electron transportation. After 400 cycles, the diameter of the semicircle became smaller and the long line became more sloping, which indicated the lower resistance and faster ion diffusion rate. This phenomenon may be ascribed to the irreversible reaction during discharge/charge progress, which will lead to the formation of metallic Fe or the activation of the electrode material and the formation of channels for the diffusion of lithium ions [55, 56]. Moreover, the existence of oxygen vacancies in the materials also could suppress the formation of insulated Li_2O, which will lower the resistance.

Conclusions

In conclusion, α-$Fe_2O_{3-\delta}$ nanoparticles with oxygen vacancies were successfully synthesized by a two-step method incorporating a sol–gel process and following calcination of the precursor. The introduction of oxygen vacancies into hematite exerts positive impact on the electrochemical performance of the final product. The as-prepared α-$Fe_2O_{3-\delta}$ shows enhanced electrochemical performance and cycling stability when being used as anode materials for LIBs. The existence of oxygen vacancies not only provides more space for Li^+ storage but also facilitates the transformation of electronic structure. Meanwhile, the introduction of oxygen vacancies could also lower the contact resistance and charge transfer resistance during the discharge/charge process, leading to the enhanced electrochemical performance of the sample.

Additional File

Additional file 1: Fig. S1. Typical XRD pattern of the precursor (a) and the corresponding TEM image (b). **Fig. S2** FT-IR spectra of the acrylic acid monomer and as-prepared precursor. **Fig. S3** Nitrogen adsorption–desorption isotherm and the corresponding pore size distribution (inset) of the as-prepared $Fe_2O_{3-\delta}$. **Fig. S4** Nyquist plots of $Fe_2O_{3-\delta}$ and commerical Fe_2O_3 before cycling and after 400 cycles at 2 C in the frequency range from 100 kHz to 0.01 Hz. (DOCX 3150 kb)

Acknowledgements
The financial support of the Natural Science Foundation of China (NSFC 21101091, 21171007, 21671005) and the Programs for Science and Technology Development of Anhui Province (1501021019) is gratefully acknowledged.

Authors' Contributions
PYZ prepared the manuscript and carried out the experiment. YWL, JWL, WWW, and ZF helped in the technical support for the characterizations. ZF designed the experiment. YYZ and XXW participated in the experiment. All the authors discussed the results and approved the final manuscript.

Competing Interests
The authors declare that they have no competing interests.

Author details
[1]Key Laboratory of Functional Molecular Solids, Ministry of Education, Center for Nano Science and Technology, College of Chemistry and Materials Science, Anhui Normal University, Wuhu 241000, People's Republic of China. [2]School of Chemistry and Chemical Engineering, University of South China, Hengyang 421001, China. [3]Present address: East Beijing Road 1#, Wuhu, Anhui Province, People's Republic of China.

Received: 12 October 2016 Accepted: 9 December 2016
Published online: 05 January 2017

References
1. Poizot P, Laruelle S, Grugeon S, Dupont L, Tarascon JM (2000) Nano-sized transition-metal oxides as negative-electrode materials for lithium-ion batteries. Nature 407:496–499
2. Xu X, Cao R, Jeong S, Cho J (2012) Spindle-like mesoporous alpha-Fe_2O_3 anode material prepared from MOF template for high-rate lithium batteries. Nano Lett 12:4988–91
3. Zhang L, Wu HB, Lou XW (2013) Metal-organic-frameworks-derived general formation of hollow structures with high complexity. J Am Chem Soc 135:10664–10672
4. Zhang L, Wu HB, Madhavi S, Hng HH, Lou XW (2012) Formation of Fe_2O_3 microboxes with hierarchical shell structures from metal-organic frameworks and their lithium storage properties. J Am Chem Soc 134:17388–17391
5. Kim J, Chung MK, Ka BH, Ku JH, Park S, Ryu J, Oh SM (2010) The role of metallic Fe and carbon matrix in Fe_2O_3/Fe/carbon nanocomposite for lithium-ion batteries. J Electrochem Soc 157:A412–A417
6. Liu J, Zhou W, Lai L, Yang H, Hua Lim S, Zhen Y, Yu T, Shen Z, Lin J (2013) Three dimensionals α-Fe_2O_3/polypyrrole (Ppy) nanoarray as anode for micro lithium ion batteries. Nano Energy 2:726–732
7. Jeong JM, Choi BG, Lee SC, Lee KG, Chang SJ, Han YK, Lee YB, Lee HU, Kwon S, Lee G, Lee CS, Huh YS (2013) Hierarchical hollow spheres of Fe_2O_3@polyaniline for lithium ion battery anodes. Adv Mater 25:6250–6255
8. Zhang L, Wu HB, Xu R, Lou XW (2013) Porous Fe_2O_3 nanocubes derived from MOFs for highly reversible lithium storage. CrystEngComm 15:9332–9335
9. Chen L, Xu H, Li L, Wu F, Yang J, Qian YT (2014) A comparative study of lithium-storage performances of hematite: nanotubes vs. nanorods. J Power Sources 245:429–435
10. Liu H, Wang GX (2014) An investigation of the morphology effect in Fe_2O_3 anodes for lithium ion batteries. J Mater Chem A 2:9955–9959
11. Cao K, Jiao L, Liu H, Liu Y, Wang Y, Guo Z, Yuan H (2015) 3D hierarchical porous α-Fe_2O_3 nanosheets for high-performance lithium-ion batteries. Adv Energy Mater 5:1401421
12. Wang Z, Luan D, Madhavi S, Hu Y, Lou XW (2012) Assembling carbon-coated α-Fe_2O_3 hollow nanohorns on the CNT backbone for superior lithium storage capability. Energy Environ Sci 5:5252–5256
13. Zhang HW, Zhou L, Noonan O, Martin DJ, Whittaker AK, Yu CZ (2014) Tailoring the void size of iron oxide@carbon yolk-shell structure for optimized lithium storage. Adv Funct Mater 24:4337–4342

14. Gu X, Chen L, Liu S, Xu H, Yang J, Qian YT (2014) Hierarchical core–shell α-Fe_2O_3@C nanotubes as a high-rate and long-life anode for advanced lithium ion batteries. J Mater Chem A 2:3439–3444
15. Li N, Du K, Liu G, Xie YP, Zhou GM, Zhu J, Li F, Cheng HM (2013) Effects of oxygen vacancies on the electrochemical performance of tin oxide. J Mater Chem A 1:1536–1539
16. Song H, Jeong TG, Moon YH, Chun HH, Chung KY, Kim HS, Cho BW, Kim YT (2014) Stabilization of oxygen-deficient structure for conducting $Li_4Ti_5O_{12-\delta}$ by molybdenum doping in a reducing atmosphere. Sci Rep 4:4350
17. Zhang J, Zhang L, Zhang J, Zhang Z, Wu Z (2015) Effect of surface/bulk oxygen vacancies on the structure and electrochemical performance of TiO_2 nanoparticles. J Alloys Compd 642:28–33
18. Xu Y, Zhou M, Wang X, Wang C, Liang L, Grote F, Wu M, Mi Y, Lei Y (2015) Enhancement of sodium ion battery performance enabled by oxygen vacancies. Angew Chem Int Ed 54:8768–8771
19. Yang TY, Kang HY, Sim U, Lee YJ, Lee JH, Koo B, Nam KT, Joo YC (2013) A new hematite photoanode doping strategy for solar water splitting: oxygen vacancy generation. Phys Chem Chem Phys 15:2117–2124
20. Chen L, Jiang X, Wang N, Yue J, Qian Y, Yang J (2015) Surface-amorphous and oxygen-deficient $Li_3VO_{4-\delta}$ as a promising anode material for lithium-ion batteries. Adv Sci 2:10500090
21. Ventosa E, Chen P, Schuhmann W, Xia W (2012) CNTs grown on oxygen-deficient anatase $TiO_{2-\delta}$ as high-rate composite electrode material for lithium ion batteries. Electrochem Commun 25:132–135
22. Peng X, Zhang X, Wang L, Hu L, Cheng SH-S, Huang C, Gao B, Ma F, Huo K, Chu PK (2016) Hydrogenated V_2O_5 nanosheets for superior lithium storage properties. Adv Funct Mater 26:784–791
23. Balogun MS, Li C, Zeng YX, Yu MH, Wu QL, Wu MM, Lu XH, Tong YX (2014) Titanium dioxide@titanium nitride nanowires on carbon cloth with remarkable rate capability for flexible lithium-ion batteries. J Power Sources 272:946–953
24. Balogun MS, Wu Z, Luo Y, Qiu WT, Fan XL, Long B, Huang M, Liu P, Tong YX (2016) High power density nitridated hematite (α-Fe_2O_3) nanorods as anode for high-performance flexible lithium ion batteries. J Power Sources 308:7–17
25. Balogun MS, Zhu YK, Qiu WT, Luo Y, Huang YC, Liang CL, Lu XH, Tong YX (2015) Chemically lithiated TiO_2 heterostructured nanosheet anode with excellent rate capability and long cycle life for high-performance lithium-ion batteries. ACS Appl Mater Interfaces 7:25991–26003
26. Brumbarov J, Vivek JP, Leonardi S, Valero-Vidal C, Portenkirchner E, Kunze-Liebhäuser J (2015) Oxygen deficient, carbon coated self-organized TiO_2 nanotubes as anode material for Li-ion intercalation. J Mater Chem A 3: 16469–16477
27. Kuscer D, Bakaric T, Kozlevcar B, Kosec M (2013) Interactions between lead-zirconate titanate, polyacrylic acid, and polyvinyl butyral in ethanol and their influence on electrophoretic deposition behavior. J Phys Chem B 117:1651–1659
28. Cho YS, Burdick VL, Amarakoon VRW (1999) Synthesis of nanocrystalline lithium zinc ferrites using polyacrylic acid, and their initial densification. J Am Ceram Soc 82:1416–1420
29. Ward LJ, Schofield WCE, Badyal JPS, Goodwin AJ, Merlin PJ (2003) Atmospheric pressure plasma deposition of structurally well-defined polyacrylic acid films. Chem Mater 15:1466–1469
30. de Faria DLA, Silva SV, de Oliveira MT (1997) Raman microspectroscopy of some iron oxides and oxyhydroxides. J Raman Spectrosc 28:873–878
31. Cao H, Wang G, Zhang L, Liang Y, Zhang S, Zhang X (2006) Shape and magnetic properties of single-crystalline hematite (alpha-Fe_2O_3) nanocrystals. Chemphyschem 7:1897–1901
32. Hassan MF, Rahman MM, Guo ZP, Chen ZX, Liu HK (2010) Solvent-assisted molten salt process: a new route to synthesise α-Fe_2O_3/C nanocomposite and its electrochemical performance in lithium-ion batteries. Electrochim Acta 55:5006–5013
33. Cho YS, Huh YD (2009) Preparation of hyperbranched structures of alpha-Fe_2O_3. Bull Korean Chem Soc 30:1413–1415.
34. Chen M, Liu J, Chao D, Wang J, Yin J, Lin J, Fan HJ, Shen ZX (2014) Porous α-Fe_2O_3 nanorods supported on carbon nanotubes-graphene foam as superior anode for lithium ion batteries. Nano Energy 9:364–372
35. Sun Z, Xie K, Li ZA, Sinev I, Ebbinghaus P, Erbe A, Farle M, Schuhmann W, Muhler M, Ventosa E (2014) Hollow and yolk-shell iron oxide nanostructures on few-layer graphene in Li-ion batteries. Chem Eur J 20:2022–2030
36. Brundle CR, Chuang TJ, Wandelt K (1977) Core and valence level photoemission studies of iron oxide surfaces and the oxidation of iron. Surf Sci 68:459–468
37. Sun Z, Madej E, Genc A, Muhler M, Arbiol J, Schuhmann W, Ventosa E (2016) Demonstrating the steady performance of iron oxide composites over 2000 cycles at fast charge-rates for Li-ion batteries. Chem Commun (Camb) 52:7348–7351
38. Moulder JF, Stickle WF, Sobol PE, Bomben KD (1992) Handbook of X-ray photoelectron spectroscopy, Physical Electronics Division, Perkin-Elmer Corporation. PerkinElmer Corporation, Eden Prairie
39. Lu X, Zeng Y, Yu M, Zhai T, Liang C, Xie S, Balogun MS, Tong Y (2014) Oxygen-deficient hematite nanorods as high-performance and novel negative electrodes for flexible asymmetric supercapacitors. Adv Mater 26:3148–3155
40. Lu X, Wang G, Zhai T, Yu M, Gan J, Tong Y, Li Y (2012) Hydrogenated TiO_2 nanotube arrays for supercapacitors. Nano Lett 12:1690–1696
41. Fujii T, de Groot FMF, Sawatzky GA, Voogt FC, Hibma T, Okada K (1999) In situ XPS analysis of various iron oxide films grown by NO_2-assisted molecular-beam epitaxy. Phys Rev B 59:3195–3202
42. McCafferty E, Wightman JP (1998) Determination of the concentration of surface hydroxyl groups on metal oxide films by a quantitative XPS method. Surf Interface Anal 26:549–564
43. Alvarez G, Font R, Portelles J, Raymond O, Zamorano R (2009) Paramagnetic resonance and non-resonant microwave absorption in iron niobate. Solid State Sci 11:881–884
44. Jitianu A, Crisan M, Meghea A, Rau I, Zaharescu M (2002) Influence of the silica based matrix on the formation of iron oxide nanoparticles in the Fe_2O_3–SiO_2 system, obtained by sol–gel method. J Mater Chem 12:1401–1407
45. Luo Y, Balogun MS, Qiu W, Zhao R, Liu P, Tong Y (2015) Sulfurization of FeOOH nanorods on a carbon cloth and their conversion into Fe_2O_3/Fe_3O_4-S core-shell nanorods for lithium storage. Chem Commun (Camb) 51:13016–13019
46. Wang B, Chen JS, Wu HB, Wang Z, Lou XW (2011) Quasiemulsion-templated formation of alpha-Fe_2O_3 hollow spheres with enhanced lithium storage properties. J Am Chem Soc 133:17146–17148
47. Yu WJ, Hou PX, Li F, Liu C (2012) Improved electrochemical performance of Fe_2O_3 nanoparticles confined in carbon nanotubes. J Mater Chem 22:13756–13763
48. Xiao W, Zhou J, Yu L, Wang D, Lou XW (2016) Electrolytic formation of crystalline silicon/germanium alloy nanotubes and hollow particles with enhanced lithium-storage properties. Angew Chem Int Ed Engl 55:7427–7431
49. Wang S, Xia L, Yu L, Zhang L, Wang H, Lou XW (2016) Free-standing nitrogen-doped carbon nanofiber films: integrated electrodes for sodium-ion batteries with ultralong cycle life and superior rate capability. Adv Energy Mater 6:1502217
50. Zeng PY, Wang XX, Ye M, Ma QY, Li JW, Wang WW, Geng BY, Fang Z (2016) Excellent lithium ion storage property of porous $MnCo_2O_4$ nanorods. RSC Adv 6:23074–23084
51. Zhu X, Song X, Ma X, Ning G (2014) Enhanced electrode performance of Fe_2O_3 nanoparticle-decorated nanomesh graphene as anodes for lithium-ion batteries. ACS Appl Mater Interfaces 6:7189–7197
52. Yu L, Zhang L, Wu HB, Lou XW (2014) Formation of $Ni_xCo_{3-x}S_4$ hollow nanoprisms with enhanced pseudocapacitive properties. Angew Chem Int Ed 53:3711–3714
53. Hu Z, Wang L, Zhang K, Wang J, Cheng F, Tao Z, Chen J (2014) MoS_2 nanoflowers with expanded interlayers as high-performance anodes for sodium-ion batteries. Angew Chem Int Ed 47:13008–13012
54. Zhang K, Hu Z, Liu X, Tao Z, Chen J (2015) $FeSe_2$ microspheres as a high-performance anode material for Na-ion batteries. Adv Mater 27:3305–3309
55. Luo J, Liu J, Zeng Z, Ng CF, Ma L, Zhang H, Lin J, Shen ZX, Fan HJ (2013) Three-dimensional graphene foam supported Fe_3O_4 lithium battery anodes with long cycle life and high rate capability. Nano Lett 13:6136–6143
56. Sun YW, Zuo XT, Xu D, Sun DZ, Zhang XX, Zeng SY (2016) Flower-like $NiCo_2O_4$ microstructures as promising anode material for high performance lithium-ion batteries: facile synthesis and its lithium storage properties. ChemistrySelect 1:5129–5136